

Compression-induced solidification of shock-melted ceriumChristopher T. Seagle,^{1,*} Michael P. Desjarlais¹,¹ Andrew J. Porwitzky,¹ and Brian J. Jensen²¹*Sandia National Laboratories, Albuquerque, New Mexico 87185, USA*²*Los Alamos National Laboratory, Los Alamos, New Mexico 87545, USA*

(Received 2 April 2020; revised 10 July 2020; accepted 14 July 2020; published 5 August 2020)

Compression-induced solidification has been observed in cerium on nanosecond timescales. A series of experiments was conducted in Sandia National Laboratories' Z Facility in which cerium was shock melted and subsequently shocklessly, or ramp, loaded across the melt line inducing solidification. The signature of solidification manifested in the recovery of material strength and the propagation of waves at the local elastic sound velocity. Density functional theory simulations of cerium along the experimental phase-space path exhibit spontaneous freezing to a tetragonal phase at the same pressure and closely predict the observed physical properties of solid and liquid cerium near melt.

DOI: [10.1103/PhysRevB.102.054102](https://doi.org/10.1103/PhysRevB.102.054102)**I. INTRODUCTION**

Evidence for compression driven solidification has only recently been realized for low- Z systems such as water [1,2] and silicon [3], utilizing entropy-generating compression techniques on dynamic timescales. Here we report an observation of isentropic-compression-induced solidification of a high- Z (58) metal, cerium, under dynamic loading on nanosecond timescales. Cerium is an ideal metal for examining solidification during dynamic compression in part due to its well characterized shock compression response in the solid and liquid [4–7], as well as a wealth of static high-pressure equation of state [8,9] and theoretical information available [10]. In addition, cerium represents an interesting challenge for first principal calculations due to partial filling of the $4f$ shell.

Cerium exhibits a minimum in the melt line near 3 GPa [11]; like water, the liquid is denser than the solid at 1 bar [12]. For the high- Z metals, cerium also has a relatively low shock-melting stress; incipient melting begins at 10 GPa on the Hugoniot [5]. This low melting pressure on the Hugoniot, near the minimum in cerium's melt curve, suggests that isentropic compression from this shock-melted state should cross back over the melt line into the subsolidus, tetragonal-Ce [13], region of phase space. To test this hypothesis experimentally, a series of shock-ramp experiments were conducted on Sandia National Laboratories' Z Facility. Z is a pulsed power facility with exquisite control of the temporal energy deposition to targets [14]. The experiments utilized a strip-line geometry [15] with a shock-ramp pulse shape [16,17] to impart a shock, steady to 0.3 GPa which is also the uncertainty of a single pair Hugoniot state, into the cerium samples of a magnitude just above the melting pressure on the Hugoniot, and subsequently imparted a shockless compression wave into the samples to isentropically compress the liquid from the shock state.

II. METHODS**A. Experiment**

Pairs of cerium samples with initial density $\rho_0 = 6.687 \pm 0.038$ g/cm³ and of differing thicknesses (typically 0.7–1.2 mm thick with lateral dimensions of 8.0×7.3 mm), were placed on the anode and cathode (Fig. 1). This geometrical arrangement results in each sample of the pair experiencing identical loading history. Samples were backed by lithium fluoride windows. Lithium fluoride has a well characterized equation of state on and off Hugoniot [18,19], as well as a validated index of refraction model at high stress [20]. The velocities of the cerium/LiF interfaces were measured with velocity interferometer system for any reflector (VISAR) [21] using a minimum of two sensitivities per sample. Apparent velocities were reduced to true velocities using an index of refraction model for LiF [20]. Up to four pairs of samples were utilized per experiment. In some cases, the thickest sample of a pair exhibited a shock during the ramp portion of the loading due to wave steepening. In these cases, the results from a sample pair that contained a shock were discarded from further analysis.

Figure 2 shows typical true velocity histories of the cerium/LiF interfaces for a pair of samples; Fig. S1 in the Supplemental Material [22] includes all velocimetry obtained in this study. A shock jump to velocity steady within uncertainty is quickly followed by a ramp compression wave. The observed shock jump lacks any structure; the elastic precursor and wave splitting associated with the gamma-alpha phase transition are not observed because they are overdriven at this Hugoniot stress, consistent with previous studies [4]. A total of four nearly identical experiments were conducted yielding ten pairs of velocimetry data which were shockless during the ramp stage of the experiments. We note there was no clear signature of solidification in the velocimetry profiles. It is thought that densification associated with solidification will result in a “pullback” in the velocimetry profile [23]. Such a signature was not observed here, possibly because of the very small change in density on solidification estimated to be

*ctseagl@sandia.gov

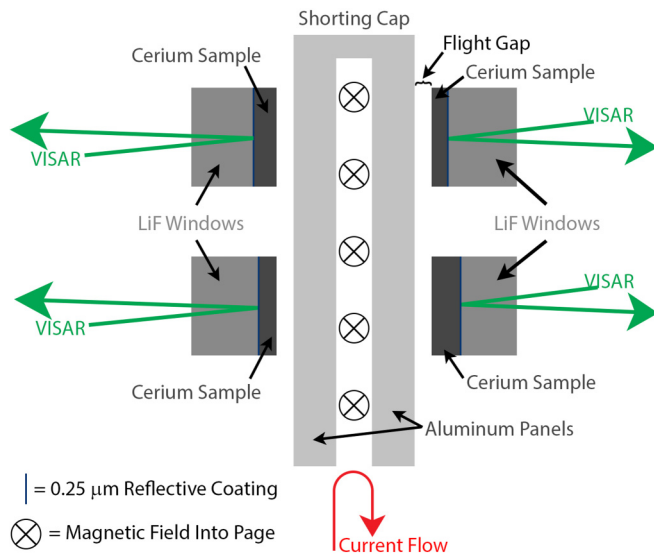


FIG. 1. Cartoon of the cerium sample arrangement on a strip-line shock-ramp target. Up to four cerium pairs per experiment were utilized (only two shown) and some experiments contained a measurement of the aluminum free surface without a sample present (Fig. S1 in the Supplemental Material [22]). The LiF windows were coated with 2500 Å of aluminum to improve reflectivity and bonded with epoxy to the cerium samples; typical bond thickness was $<2 \mu\text{m}$.

$<1\%$ based on density functional theory–molecular dynamics (DFT-MD) simulations described below. The magnitude of the shock state, averaged over ten sample pairs, is $20.6 \pm 0.1 \text{ GPa}$ at a density of $10.55 \pm 0.04 \text{ g/cm}^3$.

A dual sample hybrid backwards integration–Lagrangian analysis was utilized to determine the Lagrangian sound velocity as a function of *in situ* particle velocity [24]. These

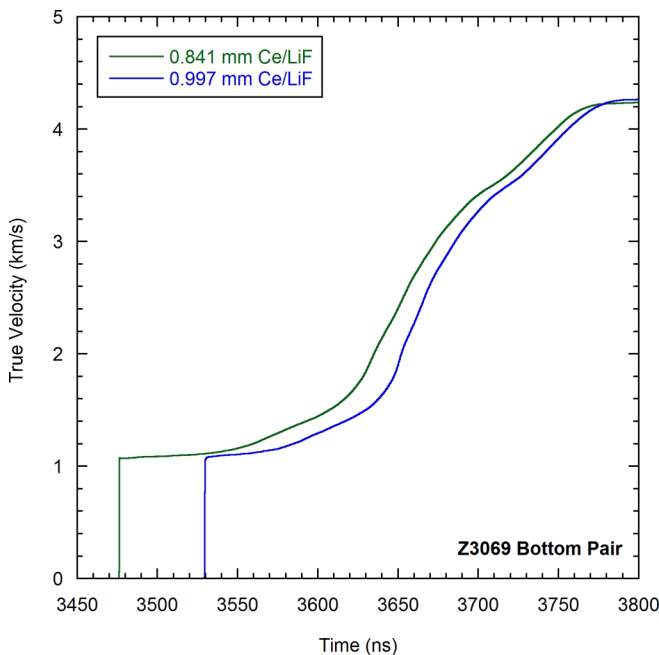


FIG. 2. Velocity of the cerium/LiF interface for one of the sample pairs on Z Experiment Z3069.

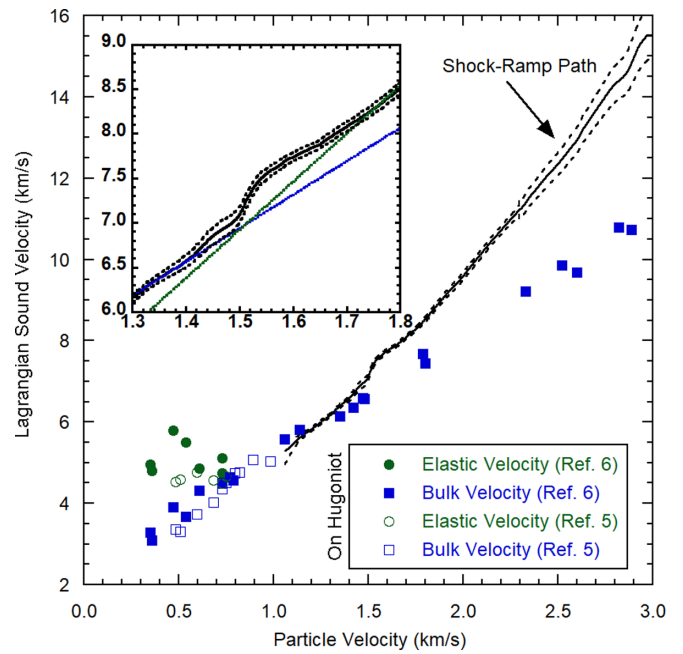


FIG. 3. Ten-sample average Lagrangian sound velocity as a function of particle velocity (solid line) and error bounds (dashed lines) along the shock-ramp path. Squares and circles are the bulk and elastic sound velocities, respectively, on the Hugoniot. Inset: detail of main figure around the bump in sound speed. Linear sound speed fit from 1.75 to 2.80 km/s particle velocity (green dashed) and from 1.05 to 1.40 km/s (blue dashed) demonstrating a change in slope near 1.5 km/s associated with solidification.

properties are state variables, which can be integrated to determine longitudinal stress and density [25]. Figure 3 shows the result of this analysis averaged over ten sample pairs obtained from four independent experiments. In each sample pair, a smooth rise in velocity is observed upon compression from the Hugoniot state; this is indicative of compression of a material without strength, such as a liquid. During ramp compression, materials with strength exhibit wave propagation at the elastic wave velocity prior to yielding, resulting in an initial decrease in apparent wave velocity with compression until the yield surface is reached, at which point waves propagate at the bulk sound velocity and increase with pressure. Similar, intentionally subsolidus, shock-ramp experiments on LiF exhibit elastic wave velocities on loading from the shock state followed by yielding to the bulk sound velocity on compression [19]; comparable elastic waves are observed for tin shocked to near the melt line [24]. The lack of an elastic wave velocity on loading from the Hugoniot state suggests that the cerium has no strength at 20.6 GPa on the Hugoniot, exactly as expected based on the known range of melting along the cerium Hugoniot [5]. In some of the experimental data obtained, a shock was observed during the ramp portion of the experiment from ~ 1.1 to 1.4 km/s particle velocity placing part of this sample on a higher-temperature isentrope compared to the companion in the pair. For this reason, and analysis difficulties that midramp shocks introduce, these pairs were discarded from analysis averaging. Figure S2 in

the Supplemental Material [22] shows individual Lagrangian velocities prior to averaging for one of the Z experiments.

A subtle bumplike feature in the Lagrangian sound velocity is observed in all ten sample pairs at 1.55 km/s particle velocity. This feature is not statistically significant on individual sample pair analyses, but consistently appears in all pair analyses. Figure 3 shows an average of ten sample pairs collected over four separate experiments. Averaging the sound velocity results in a reduction of the estimated error by a factor of 3.2. With this reduction in error, the bumplike feature at 1.55 km/s is statistically significant and represents the true response of cerium. Most materials, within a single phase, exhibit a linear increase in Lagrangian sound velocity with particle velocity (for example, LiF [26] and Ta [27]). Cerium, on this ramp compression path in the liquid, has a dichotomy in response above and below the sound velocity bump, each of which is linear but with a different slope (Fig. 3 inset). In addition, the shape of the sound velocity feature at 1.55 km/s is similar to that observed on yielding of materials during ramp compression initiating from ambient conditions (seen, for example, in Al [15] or Ta [27]). In other words, the sound velocity bump is caused by the cerium regaining strength during solidification and at this point, the local sound speed is the elastic wave velocity. Subsequent compression of the solid results in yielding, or loss of strength, and the sound velocity relaxes to the bulk sound velocity.

Assuming the feature at 1.55 km/s in the sound velocity does indeed represent an elastic wave speed and subsequent yielding, a strength analysis can be performed to estimate the magnitude of the strength, shear modulus, and Poisson ratio upon solidification. To perform this analysis, the bulk sound velocity (c_B) was linearly extrapolated down to 1.55 km/s using a linear fit to the higher-pressure response. The change in shear strength ($\Delta\tau$) upon yielding, which constrains the flow strength of the material, is related to the area between the bulk and Lagrangian (c) wave speeds [28,29]:

$$\Delta\tau = \frac{3}{4}\rho_0 \int_{u_2}^{u_1} \frac{c^2(u) - c_B^2(u)}{c(u)} du, \quad (1)$$

where u_1 and u_2 are defined as the velocity with maximum difference between the Lagrangian and bulk sound speeds and the velocity at which the Lagrangian and bulk sound speeds are equal, taken here as 1.55 and 1.75 km/s, respectively. The change in shear stress is 0.36 ± 0.09 GPa, which may be compared to the strength of cerium near ambient conditions at high strain rate, 0.13 GPa [30]. The shear modulus, G , of solid cerium after solidification at 40.8 ± 0.4 GPa and 12.03 ± 0.08 g/cm³ is 14.8 ± 3.4 GPa, which is comparable to the shear modulus of cerium at room temperature and 3 GPa (18 GPa) [8]. Using the bulk modulus, B , (211 ± 15 GPa) and shear modulus, the Poisson ratio, ν , of cerium at 40.8 ± 0.4 GPa is 0.47, very close to the upper limit of an isotropic material (liquids have a Poisson ratio of 0.5), and is in excellent agreement with the Poisson ratio during the melt transition (0.47 ± 0.2) on the Hugoniot from 10.2 to 12.6 GPa [5].

B. Theory

In light of the apparent emergence of the elastic wave signature, we have performed density functional calculations along a ramp compression path, starting from the initial experimental Hugoniot pressure of 20.6 GPa. VASP [31,32] calculations were performed with 54 cerium atoms in the supercell. The cerium atom was represented with a projector augmented wave (PAW) potential with 12 electrons in the valence [33,34]. For the DFT exchange and correlation, we used GGA+ U with PBE [35] and a U value of 1.6 eV [36]. We confirmed that this value gives very good agreement with the Olsen *et al.* diamond anvil cell data [13] for the ϵ -Ce (tetragonal) phase for pressures ranging from 14 to 46 GPa (Fig. S3 in the Supplemental Material [22]).

An estimated starting temperature of 1400 K and a density of 10.66 g/cm³ give good agreement with the experimental Hugoniot pressure and is within 1% of the experimental pressure. The isentropic-compression path from that Hugoniot starting point was simulated through a sequence of small volume compression steps at a rate of 5% per step (volume compression factor of 0.95). Temperatures were varied at each successive compression to match the initial entropy to within 1% using direct calculations of the entropy with the two-phase thermodynamic memory function (2PT-MF) method [37]. At a density of 11.8 g/cm³ and a corresponding pressure of approximately 35 GPa, we observed spontaneous freezing of the liquid within the cubic supercell. Given that this pressure would correspond to the ϵ -Ce (tetragonal) phase at ambient temperatures, we repeated these liquid simulations in a supercell with a large c/a ratio of 1.63 characteristic of the ϵ -Ce phase simulations at these temperatures. Spontaneous freezing occurred in these simulations as well near 1900 K, and was found to be the body-centered tetragonal (bct) phase characteristic of ϵ -Ce. Given the observed freezing, the isentrope for the pressure points at or above 35 GPa were computed for the solid tetragonal phase. The temperature of cerium along this isentrope is shown in Fig. S4 in the Supplemental Material [22].

Having observed the freezing to the ϵ -Ce phase, we calculate the second-order elastic constants with a set of distorted lattice calculations relative to the undistorted lattice and extract the elastic constants through differences in the stress tensor [38]. For the tetragonal phase, the six independent second-order elastic constants in Voigt notation are C_{11} , C_{12} , C_{13} , C_{33} , C_{44} , and C_{66} . We extract these through two distortions of the lattice, each applied in both contraction and dilation, for a total of four MD simulations. Since we are interested in the adiabatic elastic constants here, the temperature is also adjusted relative to the undistorted reference lattice to stay on the isentrope, again employing the direct entropy calculations.

For the body-centered tetragonal cell, we employ the two strain tensors,

$$\tilde{e}_1 = \begin{bmatrix} \delta & 0 & 0 \\ 0 & 0 & \delta/2 \\ 0 & \delta/2 & 0 \end{bmatrix} \text{ or } \tilde{e}_2 = \begin{bmatrix} 0 & \delta/2 & 0 \\ \delta/2 & 0 & 0 \\ 0 & 0 & \delta \end{bmatrix}, \quad (2)$$

with δ negative (contraction) or positive (dilation).

For cold- or low-temperature conditions, elastic constants are generally calculated with distortions of the primitive cell.

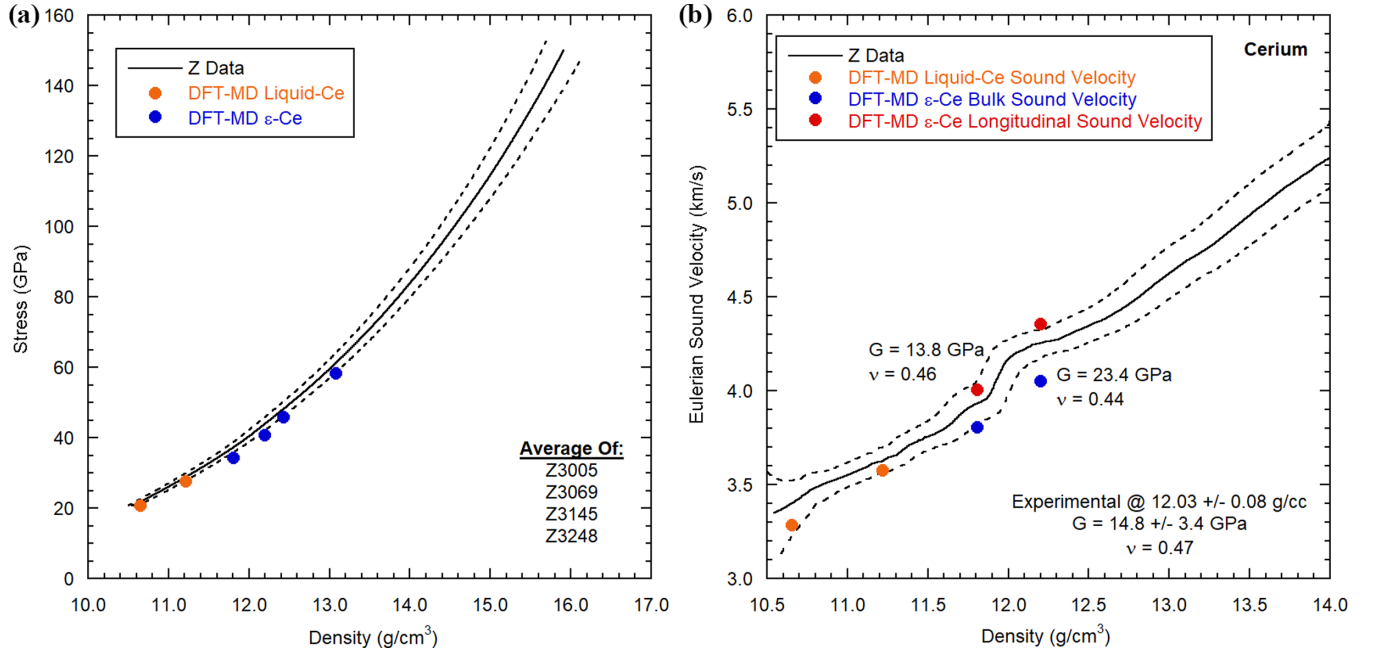


FIG. 4. (a) Stress/density (solid line) with uncertainty (dashed lines) and DFT-MD calculation results: blue circles are ϵ -Ce and orange circles are for liquid Ce. (b) Eulerian sound speed (solid line) with uncertainty (dashed lines) as a function of density with DFT-MD results: orange circles are for liquid Ce, blue circles are the ϵ -Ce bulk sound velocity, and red circles are the ϵ -Ce longitudinal sound velocity.

Since we are interested here in the elastic properties close to melt where the anharmonic content is very high, we must resort to full MD simulations. We perform the DFT molecular dynamics simulations with the deformed lattice specified by

$$\vec{a}' = (\vec{I} + \vec{\epsilon}) \cdot \vec{a}. \quad (3)$$

Through the generalized Hooke's law,

$$\sigma_{ij} = C_{ijkl} e_{kl}, \quad (4)$$

application of the first strain tensor and differencing the stresses generated with dilation and contraction ($\delta = \pm 0.01$) yields C_{11} , C_{12} , C_{13} , and C_{44} ; the second strain tensor yields C_{13} , C_{33} , and C_{66} . DFT molecular dynamics calculations with 54 atoms were performed about densities of 11.8 and 12.2 g/cm³. For these elastic constant calculations we settled on a $2 \times 2 \times 2$ Γ -centered Monkhorst-Pack k -point grid. Long simulations on the order of 10 000 time steps at 4 fs per time step were required for good convergence. We find the three independent calculations of C_{13} to be in good but not perfect agreement and take the average for the computation of the moduli and sound speeds.

We assume the emergent solid phase under ramp compression to be polycrystalline and compute the Voigt-Reuss-Hill averages for the elastic moduli and sound speeds. Results for the bulk sound speed C_B and longitudinal sound speed C_L are shown in Fig. 4 and are listed in Table I along with the bulk modulus B , shear modulus G , and Poisson ratio ν .

For comparison, we calculated the moduli and sound speeds for a perfect two-atom bct crystal at 11.81 g/cm³, but with the electronic temperature at the corresponding isentropic temperature, and using a $12 \times 12 \times 12$ Γ -centered Monkhorst-Pack k -point grid and found $B = 157$ GPa, $G = 83$ GPa, $\nu = 0.28$, $C_B = 3.639$ km/s, and $C_L = 4.747$ km/s.

This calculation also served as something of a validation for the choice of a $2 \times 2 \times 2$ Γ -centered Monkhorst-Pack k -point grid for the 54 atom molecular dynamics calculations; a perfect 54-atom bct crystal with a $2 \times 2 \times 2$ Γ -centered k -point grid gave moduli and sounds speeds that were within 1% of the highly converged ($12 \times 12 \times 12$) calculation.

III. RESULTS AND DISCUSSION

The calculated thermoelastic properties are compared to the experimental data in Figs. 4(a) and 4(b) and are in excellent agreement for both stress/density and sound velocities. The computed Poisson ratio is around 0.45, also in excellent agreement with experiment. This high level of agreement between the experimental and theoretical sound velocities, coupled with spontaneous freezing to the tetragonal phase observed in the DFT-MD simulations, strongly supports the experimental evidence for solidification during rapid isentropic compression of shock-melted cerium.

The solidification observed in these experiments and density functional calculations at around 35 GPa and 1900 K suggests a steeper high-pressure melt curve than that determined in diamond anvil cell experiments [11], but is in quite good agreement with a linear extrapolation of the high-pressure melt boundary in Ref. [5], which is based on

TABLE I. P , B , G , ν , C_B , and C_L for two densities, 11.81 and 12.20 g/cm³

ρ (g/cm ³)	P (GPa)	B (GPa)	G (GPa)	ν	C_B (km/s)	C_L (km/s)
11.81	34.3	170.9	13.8	0.46	3.804	4.004
12.20	40.7	200.3	23.4	0.44	4.052	4.356

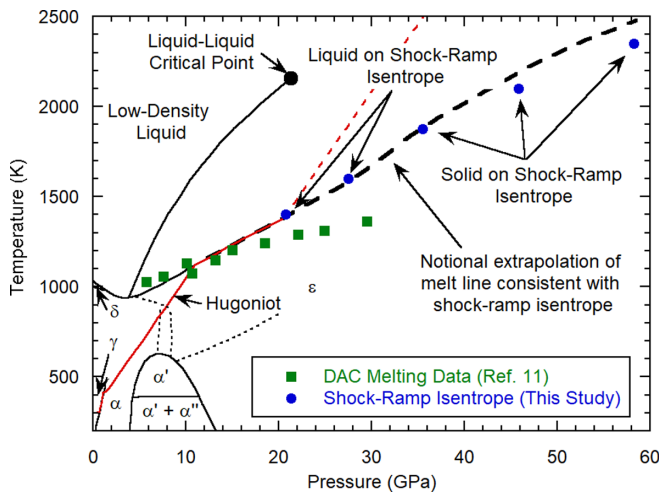


FIG. 5. Phase diagram for cerium based on Refs. [4–10,13,39,41]. Solid lines are measured phase transition boundaries. The dotted lines above the alpha-prime dome are possible alpha-epsilon phase boundary locations [42–44]—which is not well constrained with existing data. The red and red-dashed lines are the Hugoniot trajectory and a notional extrapolation of the Hugoniot trajectory consistent with existing data, respectively. Green squares are diamond anvil cell melting data [11] and blue circles are the DFT-MD results along the shock-ramp path. The black dashed line is a notional extrapolation of the melt curve consistent with the present DFT-MD results.

the equation of state developed in Ref. [39]. Figure 5 shows the experimental phase-space trajectory in the context of the cerium phase diagram. Additional melt boundary data will be required to fully resolve this discrepancy, but the experimental and theoretical data presented here are in excellent agreement; new diamond anvil cell measurements based on modern x-ray diffraction liquid scattering melt criteria may help to resolve this discrepancy.

Compression-induced solidification of metals on dynamic timescales has only recently been realized. For cerium, the first deviation from linear sound velocity increase occurs at ~ 1.45 km/s and a maximum difference between the bulk and elastic wave velocities is observed at ~ 1.55 km/s. Compression over this 0.1 km/s range occurs over 9 ns, and likely represents the timescale order of the solidification process. Here we have shown that cerium solidifies on nanosecond timescales close to the equilibrium melt line. Upon freezing, sound waves travel at the elastic wave velocity

before subsequent yielding, which can be utilized to reveal freezing and measure material properties of the solid such as the Poisson ratio at high compression near the melt line. This demonstration paves the way for rate-dependent and kinetic studies of crystallization of high- Z liquid metals subject to dynamic compression.

The elastic properties of cerium probed under dynamic compression from the liquid differ markedly from cold cerium at the same pressure. Calculations for the latter conditions reveal a Poisson ratio of 0.28 and correspondingly an elastic wave velocity much higher than the bulk velocity. We attribute the high Poisson ratio and low shear modulus observed on ramp solidification to the highly anharmonic nature of the lattice vibrations under those near-melt conditions, which is expressed primarily through a softening of the second-order elastic constant C_{66} , followed by C_{44} . Cerium under compression-induced solidification near melt is found to have a very low Pugh's ratio [40] $G/B \sim 0.1$, suggesting a highly ductile material, more so than gold, and with elastic properties differing greatly from cold cerium at comparable pressures.

ACKNOWLEDGMENTS

The authors thank two anonymous reviewers whose comments improved the quality of this manuscript. The authors thank the large and dedicated teams at Sandia and Los Alamos supporting these Z Facility experiments; this work was enabled by their efforts. C.T. Owens and J. Rivera (Los Alamos) are thanked for sample fabrication and target assembly. We thank J. Cooley for providing the well characterized cerium material. This work was supported by the U.S. Department of Energy through Sandia National Laboratories and Los Alamos National Laboratory's Science Campaign programs. This paper describes objective technical results and analysis. Any subjective views or opinions that might be expressed in the paper do not necessarily represent the views of the U.S. Department of Energy or the U.S. Government. Sandia National Laboratories is a multimission laboratory operated by National Technology and Engineering Solutions of Sandia LLC, a wholly owned subsidiary of Honeywell International Inc., for the U.S. Department of Energy's National Nuclear Security Administration under Contract No. DE-NA0003525. Los Alamos National Laboratory is operated by Triad National Security, LLC, for the National Nuclear Security Administration of the U.S. Department of Energy (Contract No. 89233218CNA000001).

[1] D. H. Dolan and Y. M. Gupta, *J. Chem. Phys.* **121**, 9050 (2004).
 [2] A. E. Gleason, C. A. Bolme, E. Galtier, H. J. Lee, E. Granados, D. H. Dolan, C. T. Seagle, T. Ao, S. Ali, A. Lazicki, D. Swift, P. Celliers, and W. L. Mao, *Phys. Rev. Lett.* **119**, 025701 (2017).
 [3] S. J. Turneaure, S. M. Sharma, and Y. M. Gupta, *Phys. Rev. Lett.* **121**, 135701 (2018).
 [4] B. J. Jensen and F. J. Cherne, *J. Appl. Phys.* **112**, 013515 (2012).
 [5] B. J. Jensen, F. J. Cherne, J. C. Cooley, M. V. Zhernokletov, and A. E. Kovalev, *Phys. Rev. B* **81**, 214109 (2010).

[6] M. V. Zhernokletov, A. E. Kovalev, V. V. Komissarov, M. G. Novikov, M. A. Zocher, and F. J. Cherne, *J. Exp. Theor. Phys.* **112**, 212 (2011).
 [7] B. J. Jensen, F. J. Cherne, and N. Velisavljevic, *J. Appl. Phys.* **127**, 095901 (2020).
 [8] M. J. Lipp, Y. Kono, Z. Jenei, H. Cynn, C. Aracne-Ruddle, C. Park, C. Kenney-Benson, and W. J. Evans, *J. Phys.: Condens. Matter* **25**, 345401 (2013).
 [9] C. Ma, Z.-Y. Dou, H.-Y. Zhi, G.-F. Fu, X. Tan, B. Bai, P.-C. Zhang, and Q.-L. Cui, *Chin. Phys. B* **25**, 046401 (2016).

- [10] V. M. Elkin, V. N. Mikhaylov, A. V. Petrovtsev, and F. J. Cherne, *Phys. Rev. B* **84**, 094120 (2011).
- [11] B. Sitaud, J. Pere, and T. Thevenin, *High Pressure Res.* **12**, 175 (1993).
- [12] W. G. Rohr, *J. Less-Common Met.* **10**, 389 (1966).
- [13] J. S. Olsen, L. Gerward, U. Benedict, and J.-P. Itie, *Physica B+C (Amsterdam)* **133**, 129 (1985).
- [14] M. E. Savage, L. F. Bennett, D. E. Bliss, W. T. Clark, R. S. Coats, J. M. Elizondo, K. R. LeChien, H. C. Harjes, J. M. Lehr, J. E. Maenchen, D. H. McDaniel, M. F. Pasik, T. D. Pointon, A. C. Owen, D. B. Seidel, D. L. Smith, B. S. Stolzhus, K. W. Struve, W. A. Stygar, L. K. Warne *et al.*, in *Proceedings of Pulsed Power Conference, 2007, 16th IEEE International (IEEE, New York, 2007)*, Vol. 2, p. 979.
- [15] J.-P. Davis, *J. Appl. Phys.* **99**, 103512 (2006).
- [16] C. T. Seagle, J.-P. Davis, M. R. Martin, and H. L. Hanshaw, *Appl. Phys. Lett.* **102**, 244104 (2013).
- [17] A. J. Porwitzky, C. T. Seagle, and B. J. Jensen, *Proc. Eng.* **204**, 337 (2017).
- [18] J.-P. Davis, M. D. Knudson, L. Shulenburg, and S. D. Crockett, *J. Appl. Phys.* **120**, 165901 (2016).
- [19] C. T. Seagle, J.-P. Davis, and M. D. Knudson, *J. Appl. Phys.* **120**, 165902 (2016).
- [20] P. A. Rigg, M. D. Knudson, R. J. Scharff, and R. S. Hixson, *J. Appl. Phys.* **116**, 033515 (2014).
- [21] L. M. Barker and R. E. Hollenbach, *J. Appl. Phys.* **43**, 11 (1972).
- [22] See Supplemental Material at <http://link.aps.org/supplemental/10.1103/PhysRevB.102.054102> for additional figures and tabular experimental data.
- [23] D. H. Dolan, J. N. Johnson, and Y. M. Gupta, *J. Chem. Phys.* **123**, 064702 (2005).
- [24] C. T. Seagle and A. J. Porwitzky, in *Shock Compression of Condensed Matter–2017, Proceedings of the Conference of the American Physical Topical Group on Shock Compression Condensed Matter, AIP Conf. Proc.* No. 1979 (AIP, Melville, NY, 2018), p. 040005.
- [25] S. D. Rothman, J.-P. Davis, C. M. Robinson, K. Parker, and J. Palmer, *J. Phys. D: Appl. Phys.* **38**, 733 (2005).
- [26] T. Ao, M. D. Knudson, J. R. Asay, and J.-P. Davis, *J. Appl. Phys.* **106**, 103507 (2009).
- [27] J.-P. Davis, J. L. Brown, M. D. Knudson, and R. W. Lemke, *J. Appl. Phys.* **116**, 204903 (2014).
- [28] J. L. Brown, C. S. Alexander, J. R. Asay, T. J. Vogler, D. H. Dolan, and J. L. Belof, *J. Appl. Phys.* **115**, 043530 (2014).
- [29] H. Huang and J. R. Asay, *J. Appl. Phys.* **98**, 033524 (2005).
- [30] B. J. Jensen, F. J. Cherne, M. B. Prime, K. Fezzaa, A. J. Iverson, C. A. Carlson, J. D. Yeager, K. J. Ramos, D. E. Hooks, J. C. Cooley, and G. Dimonte, *J. Appl. Phys.* **118**, 195903 (2015).
- [31] G. Kresse and J. Hafner, *Phys. Rev. B* **47**, 558 (1993).
- [32] G. Kresse and J. Furthmüller, *Comput. Mater. Sci.* **6**, 15 (1996).
- [33] P. E. Blöchl, *Phys. Rev. B* **50**, 17953 (1994).
- [34] G. Kresse and D. Joubert, *Phys. Rev. B* **59**, 1758 (1999).
- [35] J. P. Perdew, K. Burke, and M. Ernzerhof, *Phys. Rev. Lett.* **77**, 3865 (1996).
- [36] Y. Wang, L. G. Hector, H. Zhang, S. L. Shang, L. Q. Chen, and Z. K. Liu, *Phys. Rev. B* **78**, 104113 (2008).
- [37] M. P. Desjarlais, *Phys. Rev. E* **88**, 062145 (2013).
- [38] T. H. K. Barron and M. L. Klein, *Proc. Phys. Soc.* **85**, 523 (1965).
- [39] F. J. Cherne, B. J. Jensen, and V. M. Elkin, in *Shock Compression of Condensed Matter–2009, Proceedings of the Conference of the American Physical Topical Group on Shock Compression Condensed Matter, AIP Conf. Proc.* No. 1195 (AIP, Melville, NY, 2009), p. 1161.
- [40] S. F. Pugh, *Philos. Mag.* **45**, 823 (1954).
- [41] A. Cadien, Q. Y. Hu, Y. Meng, Y. Q. Cheng, M. W. Chen, J. F. Shu, H. K. Mao, and H. W. Sheng, *Phys. Rev. Lett.* **110**, 125503 (2013).
- [42] A. Schiwek, F. Porsch, and W. B. Holzapfel, *High Pressure Res.* **22**, 407 (2002).
- [43] O. B. Tsiok and L. G. Khvostantsev, *J. Exp. Theor. Phys.* **93**, 1245 (2001).
- [44] Y. Zhao and W. B. Holzapfel, *J. Alloys Compd.* **246**, 216 (1997).